The Macroscopic Entrainment Processes of Simulated Cumulus Ensemble. Part I: Entrainment Sources

CHICHUNG LIN AND AKIO ARAKAWA

Department of Atmospheric Sciences, University of California, Los Angeles, Los Angeles, California

(Manuscript received 12 January 1996, in final form 17 September 1996)

ABSTRACT

Parameterization of cumulus convection requires a model that describes the statistical properties of a cumulus ensemble under given large-scale conditions. Such a model is called a cloud model for cumulus parameterization (CMCP). It would be best if the development of a CMCP were guided by synchronous observations covering a population of clouds. Unfortunately, observations for cumulus clouds are usually confined to individual clouds, leaving many uncertainties in designing a CMCP.

In an attempt to improve the formulation of entrainment effects in a CMCP, the data simulated by a two-dimensional cloud-resolving model are used to investigate sources of entrainment into cumulus clouds. The authors first plot the Paluch diagram using the data from a nonprecipitating experiment. It is found that typical patterns on the Paluch diagram obtained by observational studies can be reproduced using the simulated data and can be interpreted in ways other than two-point mixing. The authors further examine entrainment sources through extensive trajectory analysis using the data from a precipitating experiment. We find that cloud air parcels at one level usually originate from locations of various heights, indicating a continuous series of entrainment events occurring throughout the cloud depth. However, the authors do not find a cloud air parcel descending more than several hundred meters. Penetrative downdrafts produced by mixing between cloud air and entrained air are not observed in the cases simulated. It seems that, as far as tropical deep convection is concerned, ignoring the contribution from descendent cloud air in a CMCP is an acceptable simplification.

1. Introduction

It is well known that cumulus convection substantially influences the behavior of large-scale circulations (e.g., Riehl and Malkus 1958). The latent heat release due to cloud processes provides the primary heat source for all tropical and many extratropical weather systems. Therefore, it is crucial to include the collective effects of cumulus clouds in the simulation of the atmosphere when individual cumulus clouds are not resolved by the model. Formulating the collective effects of such subgrid-scale cumulus clouds in terms of grid-scale prognostic variables is the problem of cumulus parameterization.

It should be emphasized, however, that cumulus parameterization is needed not only for numerical models. Understanding the interaction between moist-convective and large-scale processes is one of the most fundamental issues in the dynamics of the atmosphere, and cumulus parameterization is needed for a closed formulation of that interaction regardless of whether we are using numerical, theoretical, or conceptual models. Moreover, even if we have a numerical model that resolves all scales, initializing a simulation and interpreting its results inevitably requires various levels of ''parameterization.'' Therefore, cumulus parameterization has its own scientific merits no matter what resolution is used in numerical models.

Since cumulus parameterization is an attempt to formulate the collective effect of cumulus clouds without predicting individual clouds, it is a closure problem in which the degree of freedom is larger than the number of equations. Additional equations that govern the statistics of the system are needed to close the problem. The essence of cumulus parameterization is, therefore, in the choice of appropriate closure assumptions. In view of the uncertainties in choosing appropriate closures for cumulus parameterization, observations and other research tools should be used for directly verifying closure assumptions, for discovering improved closure assumptions, and even for assessing the limit of parameterizability; these aspects were recently addressed by Arakawa and Chen (1987), Xu et al. (1992), and Arakawa (1993).

Closures for cumulus parameterization can be derived from constraints on moist-convective processes. A cloud model for cumulus parameterization (CMCP), which determines the statistical thermodynamic properties of a cumulus ensemble under given large-scale conditions,

Corresponding author address: Dr. Chichung Lin, Dept. of Atmospheric Sciences, University of California, Los Angeles, Los Angeles, CA 90095.
E-mail: cclin@fuji.atmos.ucla.edu

provides a part of such closures. Among the CMCPs currently being used in general circulation models, the spectral cumulus ensemble model in the Arakawa–Schubert (1974) parameterization is perhaps the most comprehensive one. In this model, a single parameter, λ, is used to divide cumulus ensemble into subensembles (cloud types). It is assumed that the elements of a subensemble detrain at the same level and the detraining level of a subensemble is a monotonic function of λ. Therefore, the total mass flux in the clouds M_c can be expressed as

$$M_C(z) = \int_0^{\lambda_D(z)} m(z, \lambda)\, d\lambda, \tag{1.1}$$

where $\lambda_D(z)$ is the λ of the subensemble whose detraining level is z, and $m(z, \lambda)\, d\lambda$ is the mass flux due to subensembles whose λ are in the interval $(\lambda, \lambda + d\lambda)$. The total detrainment in the layer between z and $z + dz$, $D(z)dz$, can be related to subensemble mass flux by

$$D(z)dz = -m(z, \lambda_D(z))\, d\lambda_D(z). \tag{1.2}$$

On the other hand, the budget equations for in-cloud moist static energy, h ($h \equiv c_p T + gz + Lq_v$, where c_p is the specific heat of dry air, T the temperature, g the gravitational acceleration, z the height, L the latent heat of condensation, and q_v the mixing ratio of water vapor), and in-cloud total water, $q_v + \ell$ (ℓ is the mixing ratio of condensed water), for each subensemble can be written as

$$\frac{\partial h(z, \lambda)}{\partial z} = -\mu(z, \lambda)[h(z, \lambda) - \bar{h}(z)] \tag{1.3}$$

and

$$\frac{\partial [q_v(z, \lambda) + \ell(z, \lambda)]}{\partial z} = -\mu(z, \lambda)[q_v(z, \lambda) + \ell(z, \lambda) - \bar{q}_v(z)] - r(z, \lambda), \tag{1.4}$$

respectively, where the bar denotes the average over a large-scale horizontal unit area, r is the conversion of the liquid water to precipitation per unit height, and μ is the fractional rate of entrainment given by

$$\mu(z, \lambda) = \frac{1}{m(z, \lambda)} \frac{\partial m(z, \lambda)}{\partial z}. \tag{1.5}$$

In this way, the vertical distribution of in-cloud thermodynamic properties are determined from large-scale thermodynamical variables. It should be noted that, although (1.3) and (1.4) *formally* resemble an entraining plume, they are actually used to describe the thermodynamic properties of each subensemble rather than individual clouds. Moreover, no assumption on the vertical profile of entrainment rate is needed in deriving (1.3) and (1.4).

Effort on improving this spectral cumulus ensemble model has been continuing at the University of California, Los Angeles since the 1970s. The major modification since then is the inclusion of convective downdrafts (Cheng and Arakawa 1993, 1994). Many new questions, however, are raised even for the updraft-only model. Among them are uncertainties in formulating entrainment effects.

It has long been recognized that cumulus entrainment can significantly dilute cloud properties (Stommel 1947; Warner 1955; Squires 1958a). Squires (1958b) suggested that small cumuli were diluted mainly through penetrative downdrafts that were produced by cloud top entrainment. Squires's idea, however, did not receive much attention because, at that time, models based on the plume and thermal models were popular; most work before the 1970s concentrated on verifying or developing the plume and thermal models (e.g., Squires and Turner 1962; Simpson et al. 1965; Sloss 1967; Warner 1970; McCarthy 1974).

Many studies, however, point out problems in applying one-dimensional plume (or thermal) models to observed moist convection. For example, Warner (1970) showed that the plume model could not predict the observed mean ratio of liquid water content to its adiabatic value, W/W_a, and the cloud top height simultaneously. If sufficient entrainment was introduced to obtain the observed W/W_a, the model cloud could not reach the observed cloud top. On the other hand, if an appropriate amount of entrainment was introduced to obtain clouds reaching the observed cloud top, the model would yield excessive W/W_a. Similar conclusions were later drawn by Cotton (1975) and Betts (1982).

The community began to turn its attention to cloud top entrainment after Paluch (1979) introduced a method to infer the levels from which entrained air originates. In her analysis, cloud air properties were represented in a two-parameter space, later referred to as the Paluch diagram. The parameters chosen were wet equivalent potential temperature, θ_q, and the total water content, Q. Wet equivalent potential temperature is nearly conserved and total water content is conserved in reversible adiabatic processes. She argued that the entrainment sources could be inferred from a linear distribution of in-cloud data points on the diagram assuming two-point mixing. Applying this method to the sailplane measurements inside developing cumuli congestus in Colorado, she concluded that the entrained air originated from several kilometers above the observation level. She suggested that, as proposed by Squires (1958), the clouds were diluted mainly through the penetrative downdraft produced by cloud top entrainment.

A number of studies thereafter adopted Paluch's method or similar procedures to infer entrainment sources. Their conclusions, however, appear very different from each other. Some studies claimed that the entrained air originated near cloud top (e.g., LaMontagne and Telford 1983; Austin et al. 1985; Jensen et al. 1985; Pontikis et al. 1987; Reuter and Yau 1987),

while others reported that the entrainment sources were located near the observation level (e.g., Raymond and Wilkening 1982; Boatman and Auer 1983; Blyth et al. 1988). The former studies do not necessarily imply that the entrained air originates from a location much higher than the observation level because the observation level, for a shallow cloud in particular, can be close to cloud top. Some studies, however, did show that the entrainment sources were located several kilometers above the observation level, using the data segment taken near updraft–downdraft boundaries (e.g., Paluch 1979; Reuter and Yau 1987).

Two-point mixing, however, is not the only way to interpret the patterns on the Paluch diagram. Taylor and Baker (1991) interpreted the linear distribution of (θ_q, Q) points based on ''buoyancy sorting,'' which states that individual cloud air parcels are en route to their neutral buoyancy (Telford 1975). According to Taylor and Baker's arguments, most observed (θ_q, Q) points at one observation level would be confined to within two relatively small triangular areas in the Paluch diagram if buoyancy sorting determined in-cloud composition at each level. One of the two triangle regions corresponds to the positive buoyant mixtures between cloud-base air and environmental air below the observation level; the other corresponds to the negative buoyant mixtures between cloud-base air and environmental air above the observation level. With the data collected from the nonprecipitating clouds in Montana, they demonstrated that (θ_q, Q) points indeed fell into those triangular areas. They argued that, since these triangular areas were usually narrow, the resulting cluster of in-cloud data points would look like a straight line.

Recently Raga et al. (1990) analyzed the cumulus clouds from a trade wind region and concluded that the distribution of (θ_q, Q) points could be explained if the cloud air is the mixture of multiple sources below the observation level. They further noticed that, at levels lower than the trade inversion, almost all cloud air parcels were ascending.

As we have seen above, a number of studies have attempted to infer the levels from which entrained air originates, information that is crucial for constructing a CMCP. Most of them derived their conclusions applying Paluch's method to individual cases. From the viewpoint of cumulus parameterization, however, a dataset that covers a group of cumulus clouds would best guide the design of a CMCP. Such a dataset can be generated by a numerical cloud-resolving model (CRM), which has a large domain and resolves individual cumulus clouds. The history of CRM simulations already indicates that CRMs, with horizontal resolutions of one or a few kilometers, can reasonably simulate observed cumulus feedback on the large-scale temperature and moisture fields (Soong and Ogura 1980; Soong and Tao 1980; Tao et al. 1987; Krueger 1988; Xu et al. 1992), an objective that cumulus parameterization is intended to achieve. Moreover, it has been demonstrated that CRMs can successfully reproduce the observed vertical structure and time evolution of nonsupercellular cloud systems (Grabowski et al. 1996; Xu and Randall 1996). These facts suggest that much can be learned, for cumulus parameterization in particular, by analyzing the data generated by CRMs.

There are limitations, however, in addressing cumulus entrainment using a CRM. In view of current computer power, CRM simulations are usually restricted to two dimensions with a resolution that is much larger than turbulence scale. To evaluate the usefulness of two-dimensional cumulus entrainment simulations, we can draw upon the conclusions of studies that compared two- and three-dimensional simulations. Such comparisons have been made by Grabowski and Clark (1991, 1993a), who study moist thermals rising in a stably stratified environment using both two- and three-dimensional models with high resolutions. They conclude that the analytical theory developed to describe the evolution of the laminar interface between the thermal and its environment for two-dimensional cases can be applied to three-dimensional cases with only minor modifications. In addition, as in the two-dimensional case, the scale selection and growth rate of the unstable modes in the three-dimensional case appear to depend on the depth and velocity change across the shear layer near the interface, which is in rough agreement with the classical linear theory developed for the case of planar geometry (Asai 1970). It seems that two-dimensional simulation is still useful in obtaining insight into the problem of cumulus entrainment.

On the other hand, the limited resolution of a CRM may not allow discussions of details of cumulus entrainment process, as has been done by Klaassen and Clark (1985) and Grabowski and Clark (1991, 1993a,b). Nevertheless, it is informative to use a CRM with an optimum turbulence parameterization to simulate mass addition from the environment into clouds and then infer where the added mass comes from through trajectory analysis. The messages delivered through such an approach would be instructive for formulating entrainment effects in a CMCP. In view of the CRMs' success in simulating cumulus effects on large-scale environments, it is very likely that the entrainment process resolved by the CRM already contains the essential information needed for cumulus parameterization.

Motivated by the fact that the Paluch diagram has been extensively used to identify entrainment sources, we first analyze the data from a nonprecipitating experiment to see whether the patterns on the Paluch diagram in observational studies can be reproduced. The primary effort of this paper, however, is to infer entrainment sources of simulated deep clouds over tropical ocean. Such clouds usually produce significant precipitation, which would violate the conservation of total water, a constraint that is commonly considered necessary for inferring entrainment sources from the Paluch diagram. Therefore, trajectory analysis is used instead

to examine entrainment sources. Although calculated trajectories do not necessarily represent the actual paths of real parcels due to turbulence processes, the trajectories of the mean flow can be used as an indicator for the existence of entrainment *if they cross the cloud boundary*.

In the next section, we briefly describe the numerical experiments performed in this study, followed by some snapshots from each experiment. In section 3, we describe the methodology of analysis used in this study, including Paluch's (1979) method and trajectory analysis. Analysis results for a nonprecipitating experiment are presented in section 4, and those for a precipitating experiment are presented in section 5. The implications of these results on cumulus parameterization are discussed in section 6, and conclusions are given in section 7. The bulk characteristics of cumulus entrainment, which is perhaps the most important aspect that a CMCP needs to consider, will be addressed in Part II (Lin and Arakawa 1997) of this paper.

2. Numerical simulation of cumulus convection

a. Description of the model

In this study, we use the cloud-resolving model developed by Krueger (1988; see also Xu and Krueger 1991). The CRM is based on a two-dimensional (x–z) anelastic system of equations with the Coriolis force and a three-phase microphysical parameterization. The microphysical processes are parameterized with a bulk method following Lord et al. (1984) and Lin et al. (1983). The radiative heating rate is prescribed. The width of the domain is 256 km, and the horizontal resolution is 500 m. The depth of the model domain is 19 km with a stretched vertical coordinate. The vertical resolution is 100 m near the surface and 1 km near the top. The integration time step is 10 s. Vertical velocity is set to zero at the upper and lower boundaries, and periodic conditions are used at the lateral boundaries. At the lower boundary, the vertical turbulent fluxes of momentum, temperature, and water vapor are determined by the surface-layer wind velocity, temperature, and water vapor mixing ratio according to flux-profile relationships, following Deardorff (1972). Due to the inclusion of the Coriolis force, the y-component momentum equation is included. Variation in the y direction of all variables is ignored except for the prescribed large-scale pressure. The y-component pressure gradient is represented by a prescribed geostrophic x-component wind.

In addition to dimensionality, one drawback of studying entrainment sources using the CRM is that the resolution is incapable of resolving turbulence-scale motions, which are primarily responsible for the mixing between cloud air and environmental air. In an effort to at least partially overcome this problem, the CRM parameterizes the turbulent effects following a third-moment turbulence parameterization developed by André et al. (1978), which is expected to have a wider range of applicability than commonly used simpler parameterizations. In this parameterization, the full set of turbulence equations consists of 11 prognostic equations for second moments, 24 equations for third moments, and a diagnostic equation for the turbulent length scale (Krueger 1988). A complete description of the model's turbulence closure, including the equations, is given in Krueger (1985).

b. Experiments

Two experiments were performed with the CRM. The first experiment, A10, is designed to study cumulus clouds over a tropical ocean. The initial conditions and forcing for this experiment follow experiment Q02 in Xu et al. (1992). The initial thermodynamic profiles were taken from the Global Atmospheric Research Program (GARP) Atlantic Tropical Experiment (GATE) Phase III mean sounding and were applied to the whole domain uniformly in x. The initial wind field was in geostrophic balance with the prescribed time-independent y-component pressure gradient, which is typical of the 11 September 1974 squall line environment observed during the GATE Phase III (Sui and Yanai 1986). The lower boundary is the sea surface with a prescribed temperature of 299.9 K. The Coriolis parameter for 15° N was used. Following Xu and Krueger (1991), clouds were initiated by introducing random temperature perturbations into the lowest model layer (centered at 47 m) after 30 min of integration. Radiative cooling, large-scale advective cooling, and moistening effects were prescribed based on the situations observed in the GATE Phase III (see Fig. 1c in Xu et al. 1992). In the experiment, these effects were time independent and horizontally uniform throughout the integration. The purpose of including the large-scale advective effects is to destabilize the atmosphere and generate cumulus convection. The experiment was run for 30 h.

We find that nearly all the clouds[1] in experiment A10 have significant amounts of precipitates. Since the conservation of total water, a constraint that is commonly used for inferring entrainment sources from the Paluch diagram, is not a good approximation in this case, we turn off precipitating processes in another run, A12, which is otherwise identical to experiment A10.

It is expected that the dynamics of simulated clouds would change if precipitating processes were absent. For example, there would be no precipitation-driven convective downdrafts and no cold pool beneath (or behind) a convective system. In particular, cloud edge (or penetrative) downdrafts may be greatly enhanced due to

[1] Following Xu and Krueger (1991), an area is determined to be cloudy when the sum of mixing ratio of cloud water and cloud ice exceeds 1% of the saturation mixing ratio of water vapor.

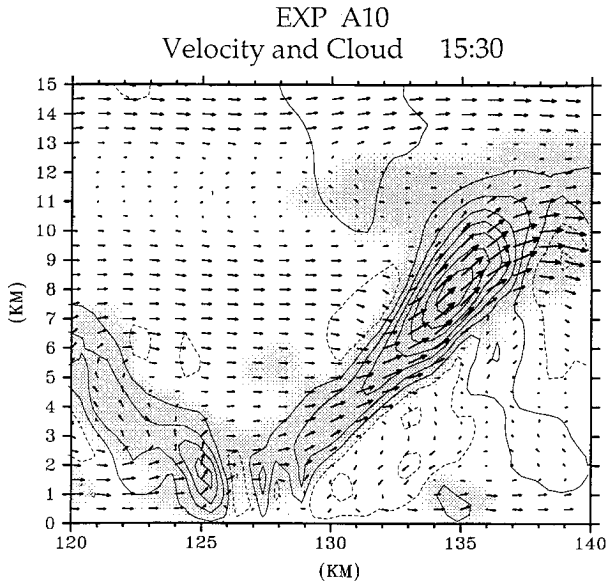

FIG. 1. Vertical cross section of clouds (shaded areas) and cloud-scale velocity (vectors) and its vertical component (contours) of a subdomain at 1530 MT in experiment A10. The cloud-scale velocity shown here is relative to the moving convective system. Solid and dashed contours show upward and downward components, respectively, with an interval of 2 m s^{-1}.

evaporation of abundant cloud droplets, which would normally precipitate when they exceed a threshold. Therefore our conclusions about the sources of cumulus entrainment will not be based on this experiment. The motivation of experiment A12 is simply to see if the patterns on the Paluch diagram in observational studies can be reproduced using the simulated data that are artificially free of precipitation.

c. Snapshots from the simulations

We first show snapshots from experiment A10 to illustrate some typical features of simulated cumulus clouds. An organized convective system forms around 1200 MT (model time) and remains a manifest feature afterwards. Such a convective system can be seen in Fig. 1, which shows cloud area, cloud-scale velocity, and its vertical component for a subdomain at 1530 MT. The convective system is moving to the left with a speed of approximately 9 m s^{-1}. The cloud-scale velocity shown is relative to a frame moving approximately with the dominant updraft, which is well shaped and tilted with an embryo cloud ahead. The cloud-scale circulation suggests that the source of the dominant updraft is from the undisturbed region ahead of the convective system. The embryo cloud, which develops into the main updraft later, forms above the convergence zone in the leading edge of the system. The dominant updraft is accompanied by three components of downdrafts; two of them are located at upper-cloud edges, and the other one penetrates into and subsequently spreads within the subcloud layer. The downdrafts are mostly outside clouds and much weaker than the updrafts.

Figure 2a shows the vertical cross sections of moist static energy, turbulent transport of moist static energy ($u''h''$,$w''h''$), and turbulent kinetic energy (TKE). (Here double primes indicate departures from resolved quantities.) We see that TKE and turbulent transport of moist static energy are large near the edges of updrafts. Turbulent transport of moist static energy is especially strong and dominated by its vertical component $w''h''$ near the upper lateral edges of tilted updrafts. The horizontal component of the transport, $u''h''$, is generally smaller than $w''h''$ but is dominant near the lower lateral edges. It is noted that the air with high moist static energy is carried up through updrafts, while the air with low moist static energy is brought down through the downdraft behind the dominant updraft. We also see that downdraft air is significantly less turbulent compared with updraft air. Similar features can also be found in Fig. 2b, which shows the mixing ratio of total water and its turbulent transports instead.

On the other hand, most of the clouds observed in experiment A12, which was run without precipitation processes, do not develop into deep convection. Figure 3 shows cloud area and cloud-scale velocity and its vertical component for a subdomain at 0330 MT. Figure 4a shows moist static energy, turbulent transport of moist static energy, and TKE; Fig. 4b shows total water, turbulent transport of total water, and TKE. Some basic features are common between the clouds in experiment A10 and those in experiment A12. Clouds are associated with updrafts; downdrafts are observed near cloud edges; TKE, turbulent transports of moist static energy, and total water are especially strong near the upper lateral edges of updrafts; and the air with high moist static energy is carried up through updrafts while the air with low moist static energy is brought down through downdrafts.

We also see different behavior between the cumulus clouds in experiment A12 and those in experiment A10. First of all, while the clouds in experiment A10 are approximately confined to updraft area (Fig. 1), the clouds in experiment A12 can extend to cloud-edge downdraft region (Fig. 3). Second, we observe much larger total water mixing ratio inside updrafts in experiment A12 than in experiment A10. [For example, the total water mixing ratio inside saturated updrafts is approximately 6–7 g kg^{-1} at the 5-km level in Fig. 2b (experiment A10), while it is 10–12 g kg^{-1} at the 5-km level in Fig. 4b (experiment A12).] Correspondingly, the gradient of total water mixing ratio across a cloud top or cloud edges in experiment A12 is also much larger than that in experiment A10. Third, while convective-scale downdrafts are exclusively located near cloud edges in experiment A12, they also appear behind (or below) the updrafts in experiment A10 (compare Fig. 3 to Fig. 1). Fourth, updrafts and downdrafts have similar magnitudes in experiment A12 but in experiment

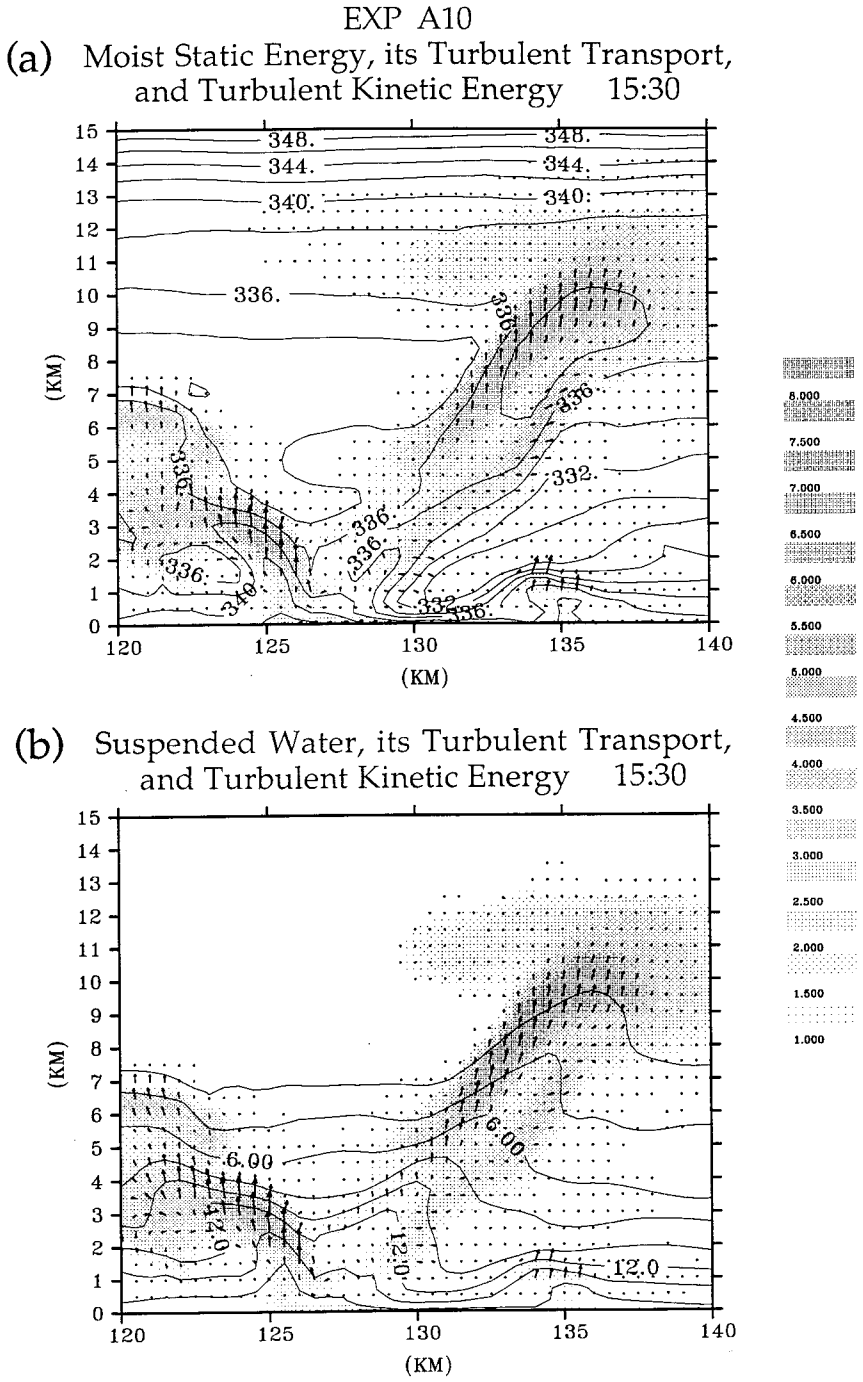

FIG. 2. (a) Vertical cross section of TKE (shades) and moist static energy h (contours), and its turbulent transport ($u''h'',w''h''$) (vectors) for the same subdomain as Fig. 1. The magnitude of TKE is indicated by a linear gray scale: white represents 0; the darkest area represents 8. Units are $m^2\ s^{-2}$ for TKE and $10^3\ m^2\ s^{-2}$ for moist static energy. The contour interval for h is $2 \times 10^3\ m^2\ s^{-2}$ and the maximum magnitudes of ($u''h'',w''h''$) is $1.66 \times 10^3\ m^3\ s^{-3}$. (b) Same as (a) except that contours are for total water mixing ratio Q, and vectors represent the turbulent transport of total water ($u''Q'',w''Q''$). Units are g kg^{-1} for mixing ratio. The contour interval for Q is 2×10^{-3} g kg^{-1}, and the maximum magnitudes of ($u''Q'',w''Q''$) is $4.12 \times 10^{-3}\ m\ s^{-1}$.

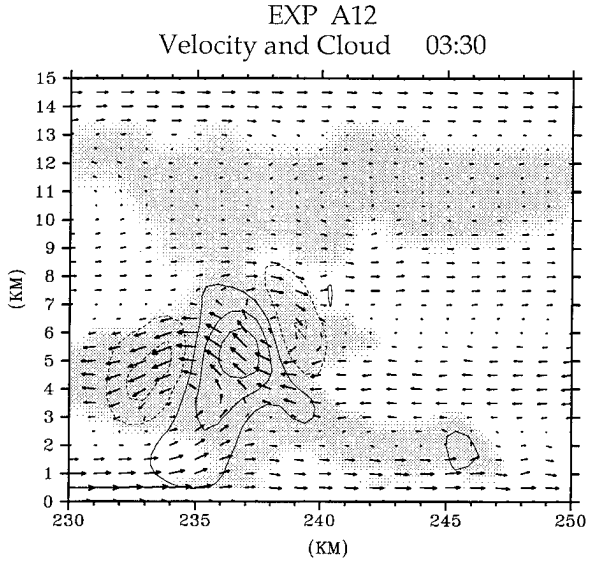

FIG. 3. Same as Fig. 1 except for a subdomain at 0330 MT in experiment A12.

A10, downdrafts are much weaker than updrafts. All of these differences are consistent with the fact that precipitating processes were absent in experiment A12.

3. Analysis methods

a. Analysis using the Paluch diagram

We use moist static energy, h, and total water,[2] Q, as the thermodynamic parameters in the Paluch diagram. Under the constraints that no ice and no precipitation are present, total water is conserved and moist static energy is approximately conserved under pseudoadiabatic processes. Paluch (1979) suggested that the linear distribution on the Paluch diagram, along with an environmental sounding, can be used to infer entrainment sources of cumulus clouds. The choice of an environmental sounding, however, can be ambiguous because different choices of environmental sounding may lead to different conclusions. Paluch points out that, in some cases, clear-air sounding is definitely not suitable for representing immediate environment of a cloud.

With simulated data, we find that the distribution of moist static energy can be used as a reference about how disturbed an area is. An absolutely undisturbed region should have horizontally uniform distribution of moist static energy. Based on this idea, we establish an objective procedure to determine the environmental sounding. In each case, we examine the rate of change of moist static energy along the horizontal direction, dh/dx, for subdomains ahead of the cloud. If dh/dx is less than 1 m s^{-2} everywhere inside a subdomain whose width is larger than 2.5 km, the mean sounding over that subdomain is used as the environmental sounding for the Paluch diagram presented.

In this study, we also examine cloud compositions through the isopleths of virtual potential temperature, θ_v, using the Paluch diagram. Here θ_v is defined as

$$\theta_v \equiv \theta(1 + 0.61q_v - q_\ell), \tag{3.1}$$

where θ is the potential temperature and q_ℓ is the mixing ratio of suspended condensate (i.e., the sum of cloud ice and cloud water). The θ_v isopleth has been used in various thermodynamic diagrams to examine the buoyancy of cloud air (e.g., Deardorff 1980; Betts 1982; Taylor and Baker 1991). Assuming that pressure is approximately constant at one level, the θ_v isopleths in (h, Q) space actually correspond to density isopleths. Therefore, we can compare the buoyancy between different air parcels once we know their locations in the Paluch diagram.

b. Trajectory analysis

For the calculation of a trajectory, linear interpolation between grid points is used to obtain the velocity of an air parcel. We then advance the position of an air parcel in time using the fourth-order Runge–Kutta scheme. To determine an appropriate time step for integration, we tested different time steps (10, 8, 6, 4, and 2 min) for a steady-state case. We find that, even for the velocity field around a severe storm with typical vertical velocity of 20 m s^{-1}, a time step of 2 min is sufficient to produce trajectories that agree with the streamlines. Thus 2-min time intervals are used in our calculation.

We also examine the budget components of moist static energy and total water mixing ratio along air parcel trajectories. The budget equation for moist static energy h can be written as

$$\frac{d}{dt}h \approx -\frac{1}{\rho_0}\nabla\cdot(\rho_0\mathbf{V}''h'') + H + R + (\partial h/\partial t)_{\mathrm{ADV}}, \tag{3.2}$$

where ρ is the density, $\mathbf{V}$ is the vector velocity, H is the latent heat release (absorption) per unit air mass due to freezing (melting), R is the radiative heating, and the subscript ADV denotes the contribution to the time derivative by large-scale advective processes. Variables with subscript 0 refer to the reference state, and double primes indicate departure from resolved quantities. The budget equation for total water mixing ratio Q can be written as

$$\frac{d}{dt}Q = -\frac{1}{\rho_0}\nabla\cdot(\rho_0\mathbf{V}''Q'') + P + (\partial Q/\partial t)_{\mathrm{ADV}}, \tag{3.3}$$

where P is the net depletion rate of total water due to precipitating processes. Along an updraft trajectory within a cumulus cloud, moist static energy is mainly changed by turbulent mixing and latent heat release (ab-

[2] In our case, total water consists of water vapor, cloud water, and cloud ice.

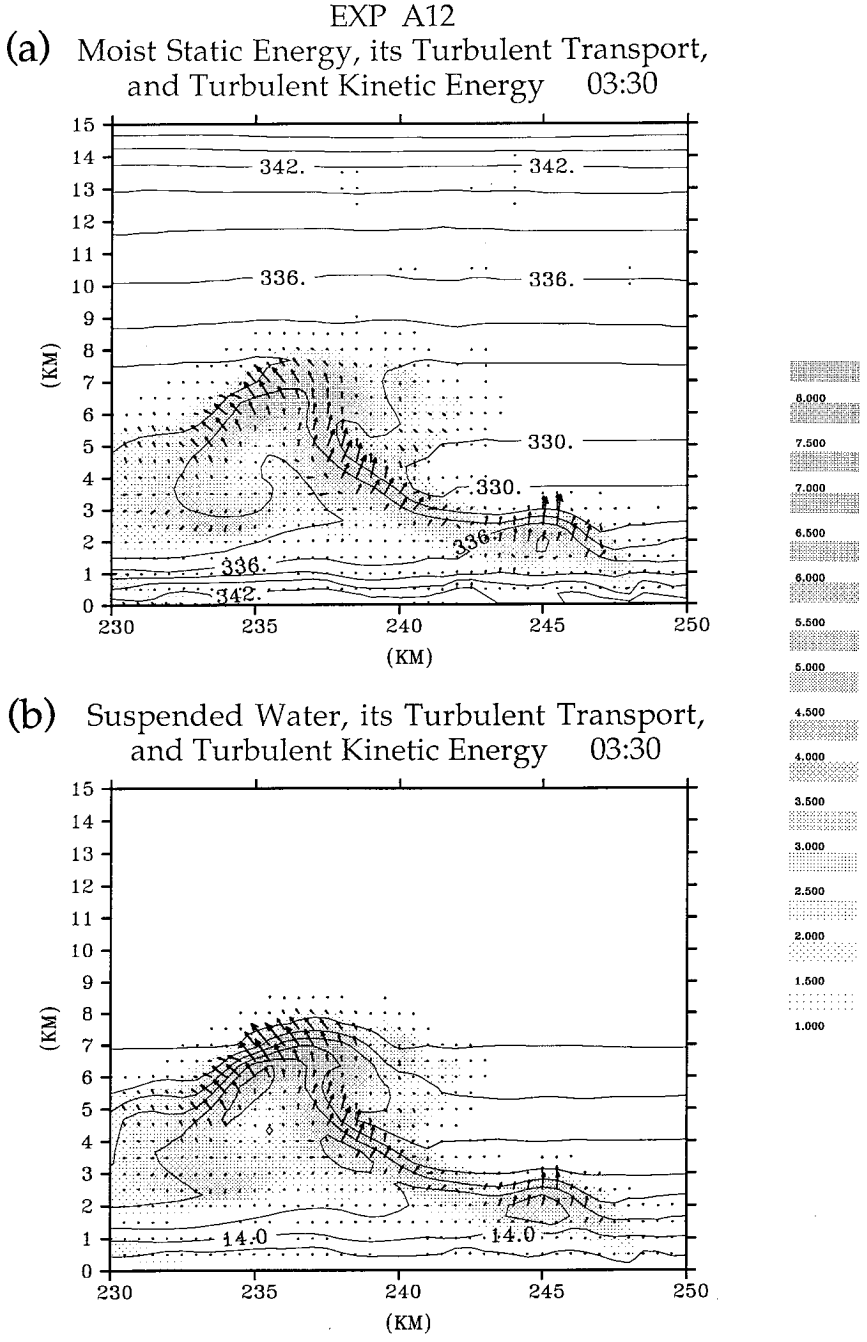

FIG. 4. Same as Fig. 2 except for a subdomain at 0330 MT in experiment A12.

sorption) due to freezing (melting), and the total water mixing ratio is mainly changed through turbulent mixing and precipitating processes.

4. Analysis of the nonprecipitating experiment A12

We first plot the (h, Q) points sampled near updraft–downdraft boundaries in the Paluch diagram. It turns out that an approximately linear distribution of (h, Q) points appear almost in every case we examined. One typical example is shown in Fig. 5. Figure 5b is the Paluch diagram with 6 consecutive data points from the 5.5-km level near one edge of the cloud in Fig. 5a. The dots in Fig. 5a correspond to the locations where data are taken. We see that the straight line passing through the data points intersect the environmental sounding at the 1.0-km and 7.0-km levels. If we follow Paluch's (1979) interpretation, we would conclude from Fig. 5b

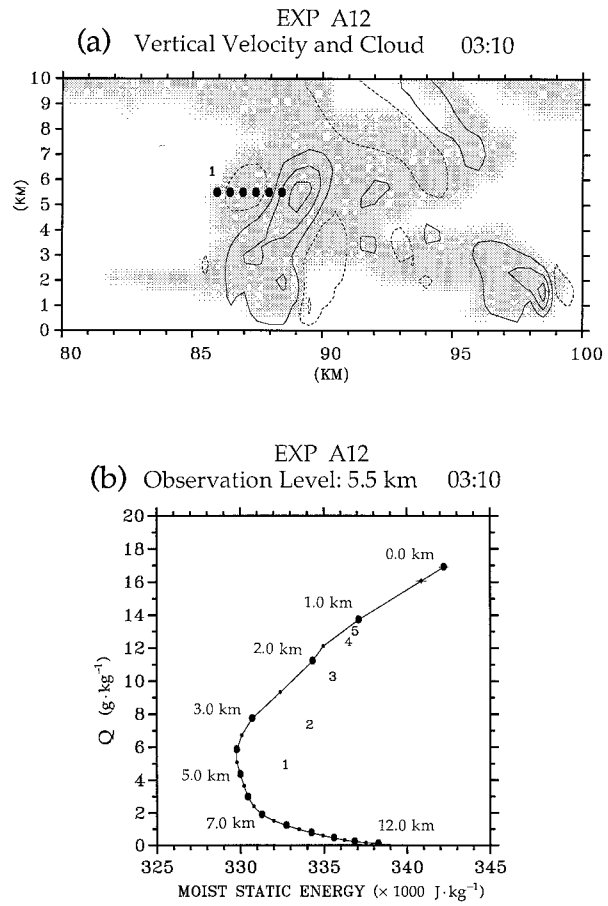

FIG. 5. (a) Vertical cross section of clouds (shades) and vertical velocity (contours) of a subdomain at 0310 MT in experiment A12. Solid and dashed contours show upward and downward velocity, respectively, with an interval of 2 m s^{-1}. The dots at the 5.5-km level represent the locations of sampling for use in the Paluch diagram. (b) Paluch diagram for the data collected at the locations indicated in (a). The abscissa is moist static energy (units: 10^3 m^2 s^{-2}), and the ordinate is the mixing ratio of total water (units: g kg^{-1}). The numbers 1, 2, 3, . . . identify the positions at which these data are collected (increasing from left to right). The environmental sounding ahead of the convective system is represented by the solid line and is labeled with height in km. The sounding is calibrated by dots. Large dots represent the 1-km, 2-km, 3-km . . . levels, and small dots represent the 0.5-km, 1.5-km, 2.5-km . . . levels.

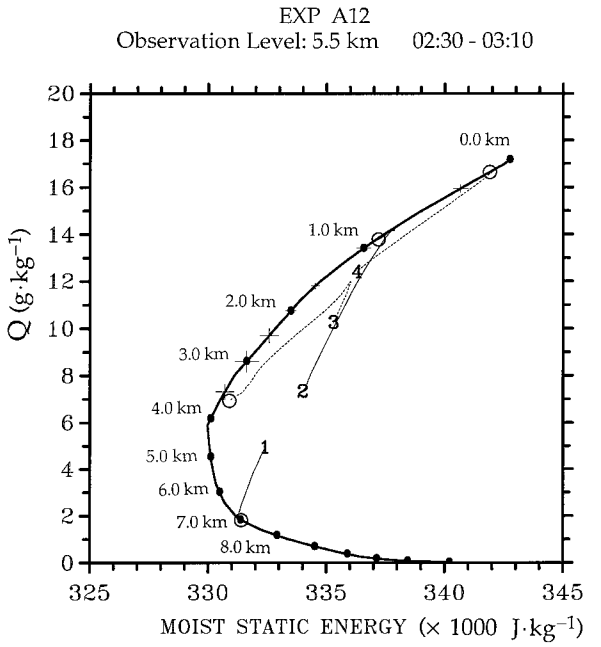

FIG. 6. Backward trajectories in the (h, Q) space for the data shown in Fig. 5b. The setting of the figure is the same as in Fig. 5b except that the environmental sounding is averaged over a period from 0230 MT to 0310 MT, with the standard deviations of moist static energy and total water within the environment indicated by horizontal bars and vertical bars, respectively. Each trajectory corresponds to one air parcel shown in Fig. 5b. The circle at one end of each trajectory locates the air parcel at 0230 MT, and the number at the other end locates the position of the air parcel at 0310 MT.

that these cloud air parcels represent the mixtures of environmental air from the 1.0-km level and from the 7.0-km level, which is significantly higher than the observation level (the 5.5-km level). To see if that is the case, we further calculated backward trajectories for the air parcels 1, 2, 3, and 4 and plotted them in the (*h*, *Q*) space as shown in Fig. 6, where each trajectory corresponds to one air parcel shown in Fig. 5b and the circle at one end of a trajectory represents the originating location of an air parcel. In Fig. 6, we see that the cloud air originates from a variety of levels.

When the isopleths of virtual potential temperature, θ_v, are superposed in Fig. 5b (see Fig. 7a), we see that the in-cloud (*h*, *Q*) points lie approximately along an isopleth of θ_v. In Fig. 7a, the thick dashed line (labeled "zero buoyancy") represents the θ_v isopleth whose value is the same as the θ_v of the environment at the observation level (the 5.5-km level). The data points located in the area to the right of the zero buoyancy line are positively buoyant, and those located in the area to the left of the zero buoyancy line are negatively buoyant. As indicated by Fig. 7a, the cloud air parcels are positively buoyant at the 5.5-km level. On the other hand, the cloud air parcels at a higher level can be negatively buoyant and still lie approximately along a θ_v-isopleth (Fig. 7b). The pattern similar to Fig. 7b had been shown by Taylor and Baker (1991) with the data sampled near the maximum cloud top. They suggested that the cluster of in-cloud points at any level should approach such a pattern as the cloud ages.

In Fig. 7a, total water mixing ratio changes from less than 5 g kg^{-1} at the cloud edge to nearly 13 g kg^{-1} at a location 2 km away from the cloud edge (the physical locations of data points in Fig. 7a can be read from Fig. 5), but the range of virtual potential temperature variation among data points is less than 0.5 K (the contour interval of virtual potential temperature in Fig. 7a is 2 K). The abrupt increase of total water across cloud boundary is a phenomenon often reported by observational studies (e.g., Warner 1955), and the limited change in virtual potential temperature is expected in

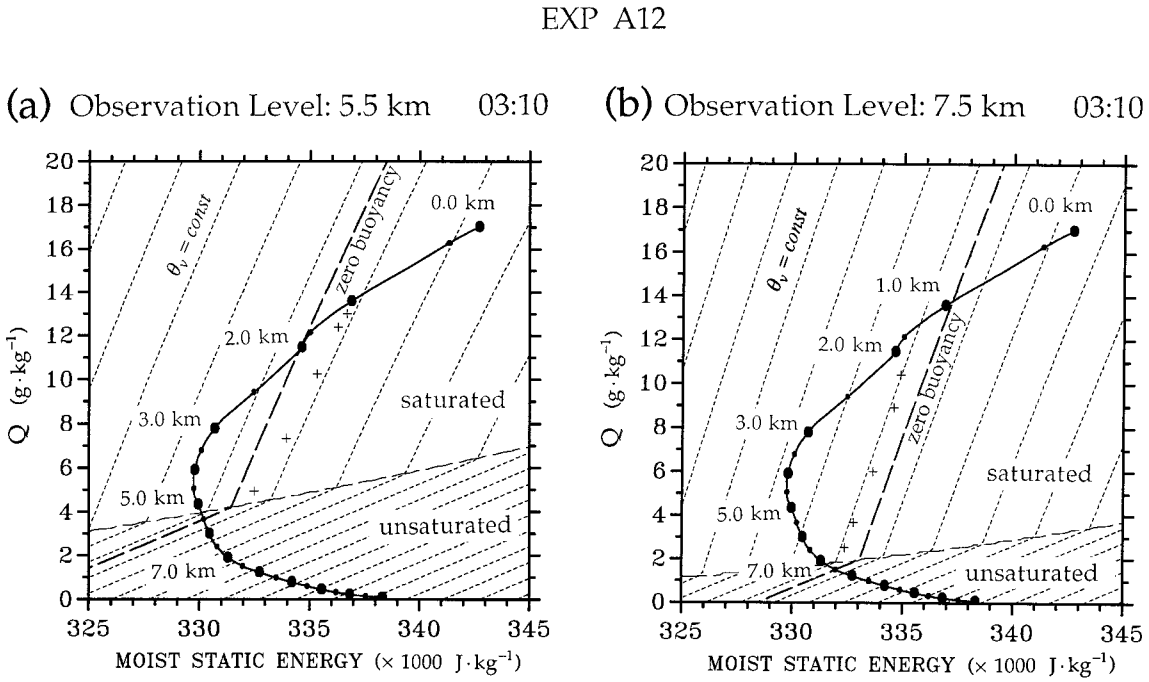

FIG. 7. Paluch diagrams for the data collected at (a) the 5.5-km level and (b) the 7.5-km level of a cloud observed at 0310 MT in experiment A12. Isopleths of virtual potential temperature (thin short-dashed lines with intervals of 2 K) are overlaid on the diagrams. In each panel, in-cloud (h, Q) is indicated by + and the zero buoyancy line is represented by the thick long-dashed line. The (h, Q) space is split into a saturated region and an unsaturated region through the thin long-dashed line.

such an area because, across cloud boundary, increases of temperature and total water tend to cancel each other in terms of contribution to virtual potential temperature. The apparent linear distribution of data points in Fig. 7a (as well as Fig. 7b) thus can be viewed as an indication that, near updraft–downdraft boundaries, variation of total water is relatively large compared to that of virtual potential temperature.

When all data points in a cloud, instead of only those sampled near updraft–downdraft boundaries, are plotted in the Paluch diagram, their distributions still resemble two-point mixing lines. Two typical examples are shown in Figs. 8a and 8b, which are the Paluch diagram with data points from the 3.5-km and the 5.5-km levels of a cloud at 0330 MT (Fig. 3). [Figures 8a and 8b are actually upside down versions of Fig. 1 in Taylor and Baker (1991).] We see that the best-fit straight line for each case intersects with the environmental sounding at two points, one of them corresponding to the height close to the observation level. If, again, we follow Paluch's (1979) interpretation, we would conclude that entrainment sources are from locations near the observation level. In fact, similar conclusions were also made by many observational studies (e.g., Raymond and Wilkening 1982; Boatman and Auer 1983; Blyth et al. 1988). However, as suggested by Taylor and Baker (1991), the patterns in Fig. 8 very probably result from the operation of buoyancy sorting. This is supported by the fact that, as argued by Taylor and Baker (1991), in-cloud (h, Q) points in Fig. 8 do tend to fall inside two narrow triangular regions, which resemble two-point mixing lines.

In summary, using the data from a nonprecipitating experiment, we can produce a Paluch diagram whose patterns are similar to those found in observational studies, and these patterns can be interpreted in ways other than two-point mixing.

5. Analysis of the tropical oceanic experiment A10

Hereafter, we do not use the Paluch diagram following Paluch's (1979) interpretation but infer entrainment sources of cumulus clouds through extensive trajectory analysis. In the following we give two examples that are typical of the cases in experiment A10.

Figure 9 shows backward trajectories in the (h, Q) space for selected air parcels sampled at the 4-km level of a cloud observed at 0740 MT. With the environmental sounding as a reference, it can be inferred that the air parcels arriving at the 4-km level of the cloud come from different levels below. The originally widely separated air parcels in the (h, Q) space come closer to each other as they ascend to the 4-km level. Along the trajectories of the air parcels originating from near the surface, h and Q decrease; along the trajectories of the air parcels originating from the environment, on the other hand, h and Q generally increase. The variations of (h, Q) along the trajectories suggest that the cloud

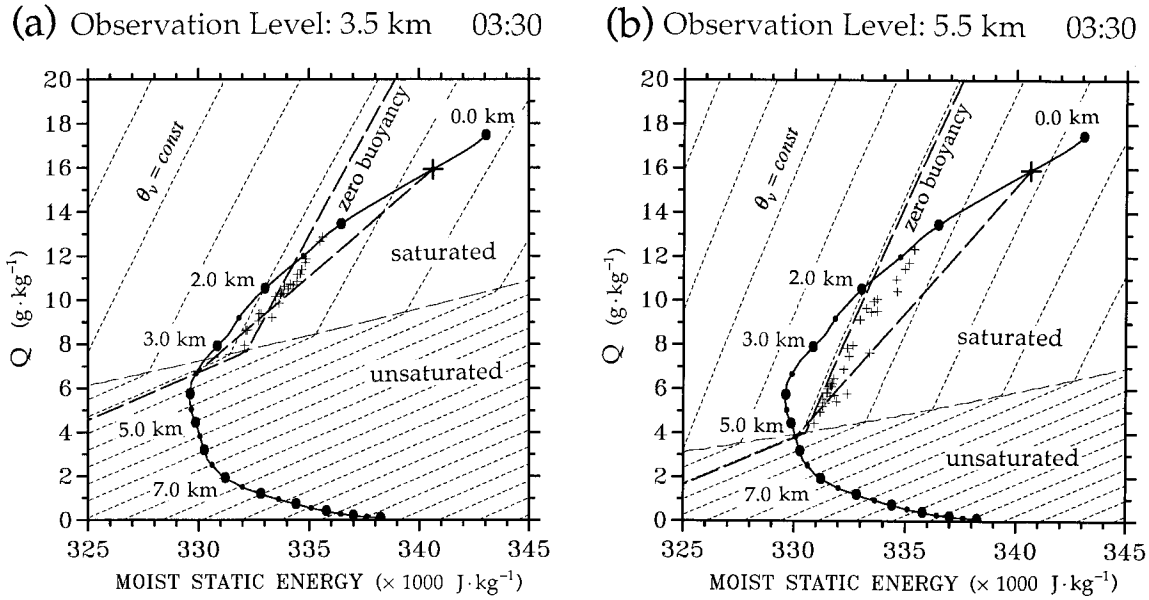

FIG. 8. Paluch diagrams for the data collected at (a) the 3.5-km level and (b) the 5.5-km level of a cloud observed at 0330 MT in experiment A12. The thick solid lines represent environmental soundings, the light dotted lines are isopleths of θ_v, the light dashed lines are saturation lines at the observation level, the thick dashed lines are the θ_v isopleths that pass through the environmental sounding at the observation level (i.e., the zero buoyancy lines), and the chain lines connect the cloud-base point (labeled by a big cross) and the point characteristic of the local environment at the observation level. The postulated cloud base (h, Q) is designated by the big cross near one end of the environmental sounding. Refer to Taylor and Baker (1991) for more detailed explanations [note that the setting of Fig. 8 is the upside down version of Taylor and Baker's (1991) figures].

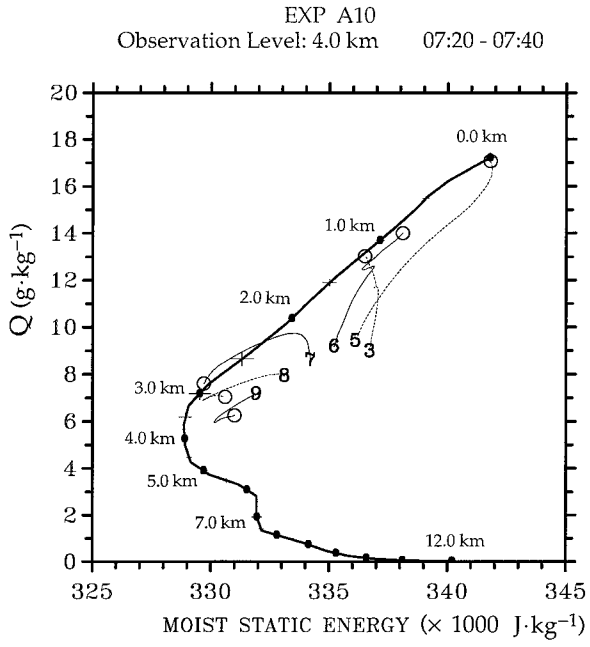

FIG. 9. Same as Fig. 6 except for selected data points sampled from the 4.0-km level of a cloud observed at 0740 MT in experiment A10. The circle at one end of each trajectory locates the air parcel at 0720 MT, and the number at the other end locates the air parcel at 0740 MT. Data points 1, 2, and 4 are omitted for clarity.

air parcels mix significantly with each other or with the environmental air. The corresponding trajectories in the physical space (with clouds and vertical velocity as background) are plotted in Fig. 10. It is observed that the cloud air parcels originate from various levels below the observation level (the 4-km level), and they never reach locations significantly higher than that level in their entire backward trajectories. This is true even for the air parcels that are located inside a cloud-edge downdraft. As shown in Fig. 10, the descents of air parcels 1 and 2 are less than 300 m.

Another example is given in Fig. 11, which shows backward trajectories in the (h, Q) space for selected air parcels sampled at the 8-km level of an organized convective system observed at 1530 MT. Again, it is found that the in-cloud data points at the observation level (the 8-km level) have widely separated origins below that level. The corresponding trajectories in the physical space (Fig. 12) also show that the cloud air parcels never reach locations higher than the observation level in their entire trajectories.

It is noted that, in both Figs. 10 and 12, some air parcel trajectories are observed crossing cloud boundaries. For example, air parcel 3 in Fig. 10 (Fig. 12) is outside clouds at 0720 MT (1440 MT) and is inside a cloud at 0740 MT (1510 MT). This indicates that entrainment should have been taking place between 0720 MT and 0740 MT (1440 MT and 1510 MT) so that the air parcel, which is originally located in the cloud en-

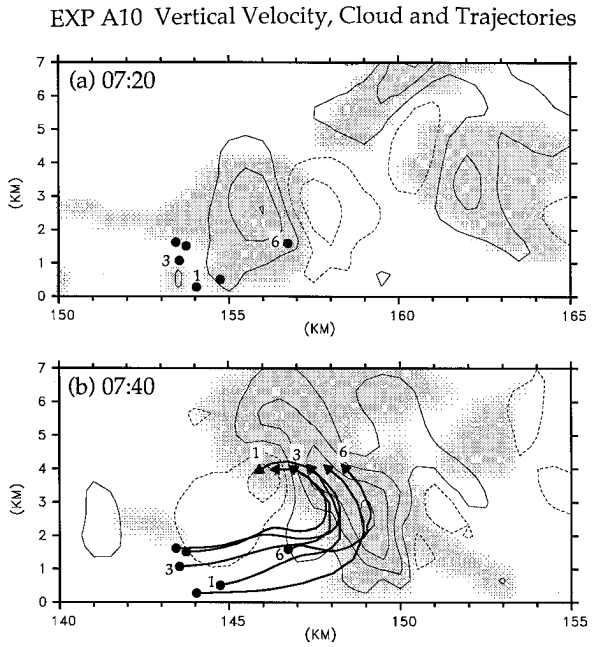

FIG. 10. Backward trajectories in the physical space for selected data points sampled from the 4.0-km level of a cloud observed at 0740 MT in experiment A10, and cross sections of clouds (shades) and vertical velocity (contours) for subdomains at (a) 0720 MT and (b) 0740 MT in experiment A10. Solid and dashed contours show upward and downward velocity, respectively, with an interval of 2 m s^{-1}. The trajectories are relative to a frame moving at the speed of the cloud and correspond to the data points in Fig. 9 through the numbers. The arrow at one end of each trajectory indicates the position of the air parcel (at the time specified in each panel), and the solid circle at the other end indicates the starting point of backward trajectory calculation.

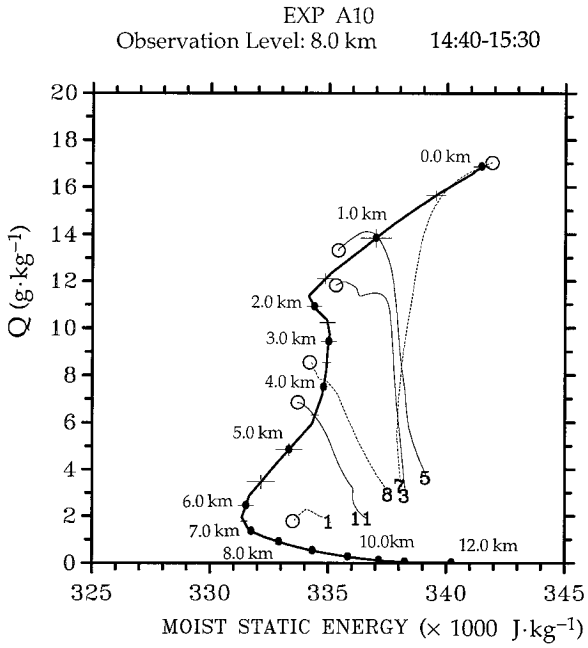

FIG. 11. Same as Fig. 9 except for selected data points sampled from the 8.0-km level of a cloud observed at 1530 MT in experiment A10. The circle at one end of each trajectory locates the air parcel at 1440 MT, and the number at the other end locates the air parcel at 1530 MT. Data points 2, 4, 6, 9, 10, and 12 are omitted for clarity.

vironment, eventually enters and becomes a part of a cloud as indicated by the trajectory.

In addition to looking at backward trajectories of cloud air parcels, we examine the moist static energy and total water budgets along individual trajectories. Here we show the results for two of them: one is for an air parcel originating from the planetary boundary layer (PBL) (air parcel 7 in Fig. 12), and the other for an air parcel originating from the cloud environment above the PBL (air parcel 3 in Fig. 12). Figures 13 and 14 show the time sequences of moist static energy, total water, and their budget components along trajectories 7 and 3, respectively. From Figs. 13 and 14, we see that air parcel 7 originally has significantly higher values of moist static energy and total water than those of air parcel 3. The vertical turbulent mixing then reduces moist static energy and total water along the trajectory of air parcel 7, but increases the moist static energy and total water along the trajectory of air parcel 3. Therefore, the inhomogeneity inside a cloud is at least partially caused by entrained air (e.g., air parcel 3) that mixes significantly but not completely with cloud air (e.g., air parcel 7) for a certain period of time after it enters the cloud.

We also notice that, in Figs. 13 and 14, the latent heat release due to ice–liquid phase change becomes important in the moist static energy budget as the air parcels approach the 8-km level, and that the total water drops dramatically near the end of the trajectory. Since there is no significant turbulent mixing at higher levels, precipitating processes are presumably responsible for causing such decrease in total water.

6. Discussion

At this point, we would like to discuss the implication of our findings on constructing a cloud model for cumulus parameterization. Recently the trend has been to believe that the dynamics of cumulus clouds is governed by buoyancy sorting. The idea was supported by Taylor and Baker (1991) and incorporated into Emanuel's (1991) cumulus parameterization scheme based on the stochastic mixing model proposed by Raymond and Blyth (1986). In Emanuel's scheme, cumulus clouds are hypothesized to be composed of discrete parcels; the mixing between each undiluted parcel and environmental air occurs in discrete events and is distributed uniformly with height. Any mixing proportion of an air parcel to the environmental air is assumed to have equal probability anywhere between cloud base and cloud top. The mixed parcels then seek their levels of ultimate neutral buoyancy and detrain from the clouds.

An important point of Emanuel's scheme is that an effective cumulus parameterization scheme should take

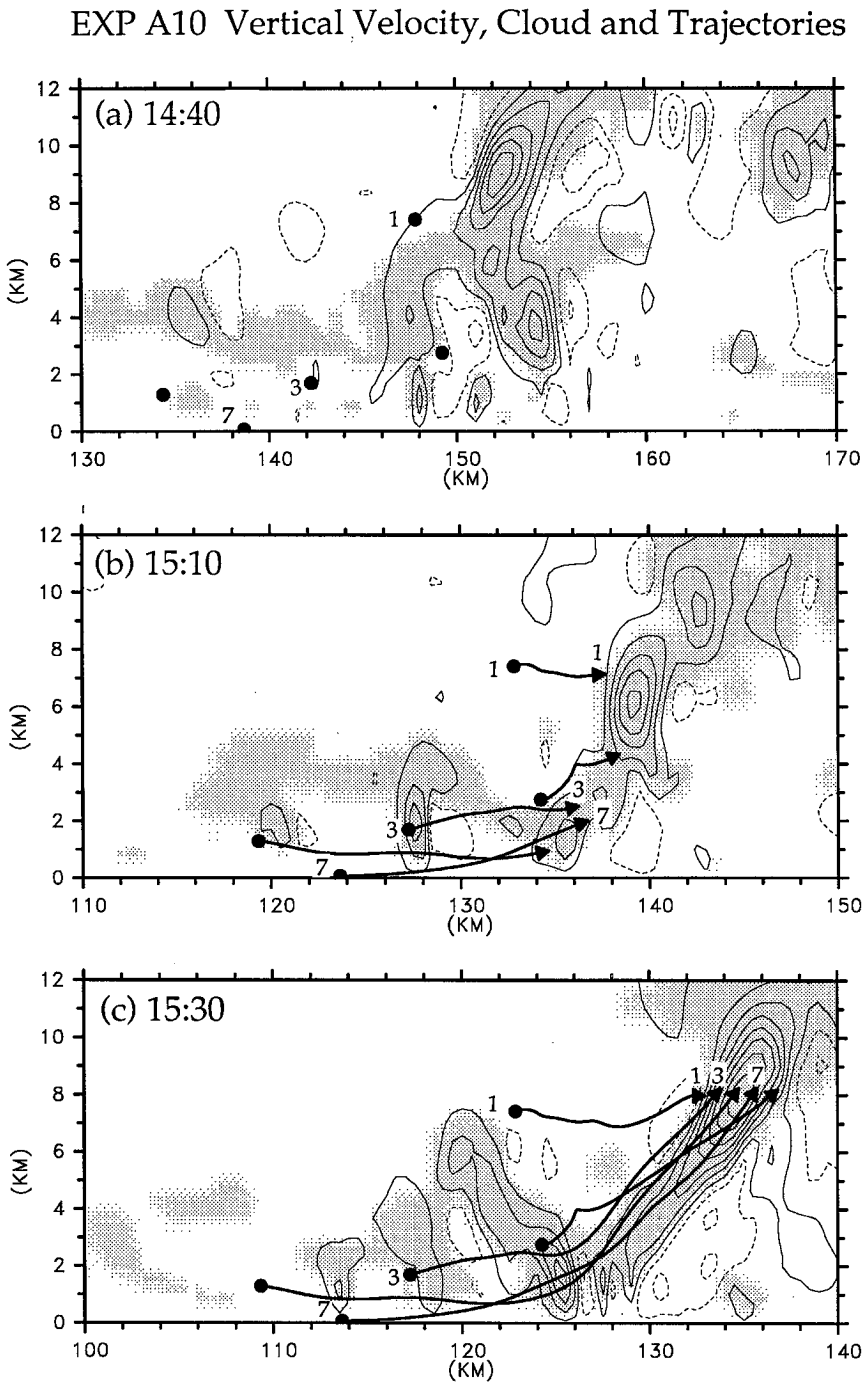

FIG. 12. Same as Fig. 10 except that the trajectories are for selected data points at the 8.0-km level of a cloud observed at 1530 MT in experiment A10, and the cross sections are for subdomains at (a) 1440 MT, (b) 1510 MT, and (c) 1530 MT. The trajectories correspond to the data points in Fig. 11 through the numbers.

into account both positive buoyant and negative buoyant cloud elements that are en route to their equilibrium states. There is no reason to exclude the possibility that mixtures of the environmental air and cloud air can descend substantially after entrainment takes place. This possibility was used to challenge the Arakawa–Schubert parameterization, which assumes that cloud elements ascend until they detrain. If, as proposed by Squires (1958), penetrative downdrafts produced by mixing between cloud air and entrained air are important processes

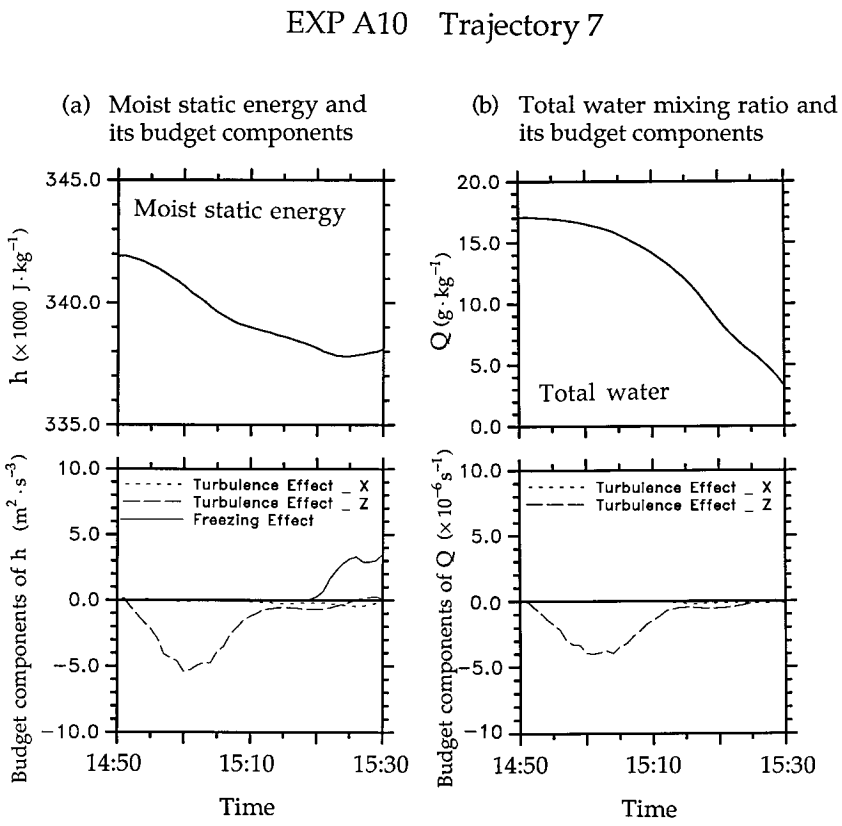

FIG. 13. Time sequences of (a) moist static energy (upper panel) and its budget components (lower panel), and (b) mixing ratio of total water (upper panel) and its budget components (lower panel) for air parcel 7 shown in Fig. 12. The abscissa is the time. Convergence of the horizontal turbulent fluxes is indicated by dotted lines, and convergence of the vertical turbulent fluxes is indicated by dashed lines. The change of moist static energy due to ice–liquid phase change is shown by the thin solid line. Units are 10^3 m^2 s^{-2} for moist static energy and m^2 s^{-3} for its budget components, and g kg^{-1} for total water mixing ratio and 10^{-6} s^{-1} for its budget components.

and dilution of clouds occurs mainly through such processes, the framework of the CMCP in the Arakawa–Schubert parameterization would be questionable.

In section 5, we showed that the sources of a cumulus cloud at one level are from locations of various heights. This is in agreement with Taylor and Baker's (1991) conclusion that a continuous series of entrainment events occurs throughout the cloud depth. We also believe that in general, as demonstrated by Taylor and Baker (1991), the positive buoyant cloud elements come from levels below and the negative buoyant cloud elements come from levels above. However, through the cases we examined, we do not find a cloud air parcel descending more than several hundred meters. In other words, cloud elements come from levels above (i.e., saturated downdrafts, which presumably resulted from entrainment) are mostly from locations close to where they are observed. Thus the framework of the spectral model used in the Arakawa–Schubert parameterization, as outlined by Eqs. (1.1)–(1.5), is not contradicted by the evidence presented in this study. It seems that *ignoring the contribution from descendent cloud air in a CMCP is an acceptable simplification* as far as tropical deep convection concerns.

7. Conclusions and summary

This study focuses upon providing a basis for formulating entrainment effects in a CMCP. The simulated data from a two-dimensional cloud-resolving model is used to investigate entrainment sources of cumulus clouds. Motivated by the fact that the Paluch diagram has been extensively used to identify entrainment sources, we analyze the data from a nonprecipitating experiment (experiment A12) to see whether the basic features of the Paluch diagram from observational studies can be reproduced using the simulated data. The main objective of this paper, however, is to infer entrainment sources for a case of tropical deep clouds over ocean in which significant precipitation is produced (experiment A10). In this case, we cannot interpret the Paluch diagram in ways that are commonly used in ob-

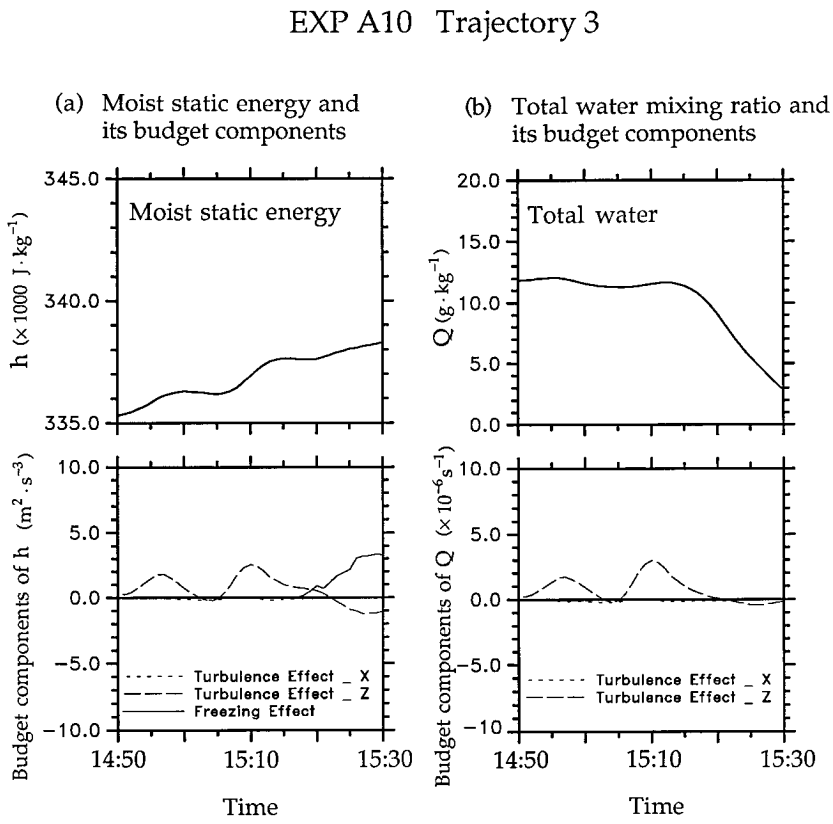

FIG. 14. Same as Fig. 13 except for air parcel 3, shown in Fig. 12.

servational studies. Entrainment sources are examined mainly through trajectory analysis.

Similarity is found between the Paluch diagram using the data from experiment A12 and that from observations. In experiment A12, a linear distribution of in-cloud data points usually appears in the Paluch diagram. Following Paluch (1979), we first attempt to interpret the patterns on the Paluch diagram as a result of mixing involving only two sources. In some cases the inferred sources are from altitudes significantly higher than the observation level. It is also very common, however, that the inferred sources are close to the observational level. Through trajectory analysis, it is shown that the approximately linear distribution of in-cloud data points in the Paluch diagram can result from mixing involving multiple sources. In addition, such a pattern can be interpreted in ways other than two-point mixing.

With the data from experiment A10, we frequently observe that air parcels that are originally located in the cloud environment eventually enter and become a part of a cloud. These air parcels usually have smaller moist static energy and total water compared to those originating from the PBL. The inhomogeneity inside a cloud is at least partially caused by such entrained air, which mixes significantly but not completely with cloud air for a certain period of time after it enters the cloud.

We also find that the sources of a cumulus cloud at one level are from locations of various heights, indicating that entrainment events occur continuously throughout the cloud depth. Nevertheless, we do not find a cloud air parcel that descends more than several hundred meters. Penetrative downdrafts produced by mixing between cloud air and entrained air, as proposed by Squires (1958), are not observed in the cases we studied. It seems that, as far as tropical deep convection is concerned, ignoring the contribution from descendent cloud air in a CMCP is an acceptable simplification.

Since this paper is based on only two experiments, the conclusions should be considered tentative and their generalizability needs to be examined through more extensive experiments covering a variety of situations. For example, the soundings from midlatitude continental regions are usually drier than those from tropical oceanic regions. This may lead to stronger negative buoyancy when environmental air is entrained into clouds. We also admit that the conclusions of this paper are derived from the induction of case studies. Although the cases we examined cover many situations (including deep organized convective systems as well as scattered small clouds), they may not be sufficient to guide the design of CMCP. The bulk characteristics of cumulus entrainment, which are perhaps the most important aspect a CMCP needs to consider, will be addressed in the companion paper (Part II).

Finally, our conclusions should not be used to deny those derived from observational studies because they may be influenced by the dimensionality and resolution of the performed simulations. It is possible that trajectory analysis may reveal entrainment sources from locations much higher than the observation level when the grid size is sufficiently small. If this indeed occurs, we have to determine the relative importance of the sources from above and those from below. In spite of all these possibilities, the results presented in this paper are instructive in view of the CRMs' success in simulating cumulus effects on large-scale environment. From the perspective of cumulus parameterization, it is very likely that the entrainment process resolved by the CRM already contains the essential information needed for cumulus parameterization.

Acknowledgments. The authors would like to thank Professor Steven Krueger and Dr. Kuan-Man Xu for their help in using the cloud-resolving model. Thanks are also extended to Professor Michio Yanai and Ms. Christine Holten for their valuable comments. We are especially grateful to Professors Steven Krueger and Nilton Rennó, Dr. Kuan-Man Xu, and two anonymous reviewers for their thorough reviews, which have led to significant improvement of the original manuscript. This material is based on work supported jointly by NSF Grant ATM-9224863, NASA Grants NAG 5-789 and 5-2591, WESTGEC Grant 91-026, and DOE CHAMMP Grant DE-FG03-91ER61214. The computations were performed at the Department of Atmospheric Sciences at UCLA and the NCAR Scientific Computing Division. NCAR is sponsored by the NSF.

REFERENCES

André, J. C., G. De Moor, P. Lacarrere, G. Therry, and R. du Vachat, 1978: Modeling the 24-hour evolution of the mean and turbulent structures of the planetary boundary layer. *J. Atmos. Sci.,* **35,** 1861–1883.

Arakawa, A., 1993: Closure assumptions in the cumulus parameterization problem. *The Representation of Cumulus Convection in Numerical Models of the Atmosphere, Meteor. Monogr.,* No. 46, Amer. Meteor. Soc., 1–16.

——, and W. H. Schubert, 1974: Interaction of a cumulus cloud ensemble with the large-scale environment. Part I. *J. Atmos. Sci.,* **31,** 674–701.

——, and J.-M. Chen, 1987: Closure assumptions in the cumulus parameterization problem. *WMO/IUGG NWP Symp. Short and Medium Numerical Prediction,* Tokyo, Japan, World Meteor. Org., 107–131.

Asai, T., 1970: Stability of a plane parallel flow with variable vertical shear and unstable stratification. *J. Meteor. Soc. Japan,* **48,** 129–138.

Austin, P. H., M. B. Baker, A. M. Blyth, and J. B. Jensen, 1985: Small-scale variability in warm continental cumulus clouds. *J. Atmos. Sci.,* **42,** 1123–1138.

Betts, A. K., 1982: Saturation point analysis of moist convective overturning. *J. Atmos. Sci.,* **39,** 1484–1505.

Blyth, A. M., W. A. Cooper, and J. B. Jensen, 1988: A study of the source of entrained air in Montana cumuli. *J. Atmos. Sci.,* **45,** 3944–3964.

Boatman, J. F., and A. H. Auer Jr., 1983: The role of cloud top entrainment in cumulus clouds. *J. Atmos. Sci.,* **40,** 1517–1534.

Cheng, M.-D., and A. Arakawa, 1993: A cumulus parameterization with rainwater budget and convective downdrafts. Preprints, *20th Conf. on Hurricane and Tropical Meteorology,* San Antonio, TX, Amer. Meteor. Soc., 313–316.

——, and ——, 1994: Effects of including convective downdrafts and a finite cumulus adjustment time in a cumulus parameterization. Preprints, *10th Conf. on Numerical Weather Prediction,* Portland, OR, Amer. Meteor. Soc., 102–104.

Cotton, W. R., 1975: On parameterization of turbulent transport in cumulus clouds. *J. Atmos. Sci.,* **32,** 548–564.

Deardorff, J. W., 1972: Parameterization of the planetary boundary layer for use in general circulation models. *Mon. Wea. Rev.,* **100,** 93–106.

——, 1980: Cloud-top entrainment instability. *J. Atmos. Sci.,* **37,** 131–147.

Emanuel, K. A., 1991: A scheme for representing cumulus convection in large-scale models. *J. Atmos. Sci.,* **48,** 2313–2335.

Grabowski, W. W., and T. L. Clark, 1991: Cloud–environment interface instability: Rising thermal calculations in two spatial dimensions. *J. Atmos. Sci.,* **48,** 527–546.

——, and ——, 1993a: Cloud–environment interface instability. Part II: Extension to three spatial dimensions. *J. Atmos. Sci.,* **50,** 555–573.

——, and ——, 1993b: Cloud–environment interface instability. Part III: Direct influence of environmental shear. *J. Atmos. Sci.,* **50,** 3821–3828.

——, X. Wu, and M. W. Moncrieff, 1996: Cloud-resolving modeling of tropical cloud systems during Phase III of the GATE. Part I: Two-dimensional experiments. *J. Atmos. Sci.,* **53,** 3684–3709.

Jensen, J. B., P. H. Austin, M. B. Baker, and A. M. Blyth, 1985: Turbulent mixing, spectral evolution and dynamics in a warm cumulus cloud. *J. Atmos. Sci.,* **42,** 173–192.

Klaassen, G. P., and T. L. Clark, 1985: Dynamics of the cloud–environment interface and entrainment in small cumuli: Two-dimensional simulations in the absence of ambient shear. *J. Atmos. Sci.,* **42,** 2621–2642.

Krueger, S. K., 1985: Numerical simulation of tropical cumulus clouds and their interaction with the subcloud layer. Ph.D. dissertation, University of California, Los Angeles, 205 pp.

——, 1988: Numerical simulation of tropical cumulus clouds and their interaction with the subcloud layer. *J. Atmos. Sci.,* **45,** 2221–2250.

LaMontagne, R. G., and J. W. Telford, 1983: Cloud top mixing in small cumuli. *J. Atmos. Sci.,* **40,** 2148–2156.

Lin, C., and A. Arakawa, 1997: The macroscopic entrainment processes of simulated cumulus ensemble. Part II: Testing the entraining-plume model. *J. Atmos. Sci.,* **54,** 1044–1053.

Lin, Y.-L., R. D. Farley, and H. D. Orville, 1983: Bulk parameterization of the snow field in a cloud model. *J. Climate Appl. Meteor.,* **22,** 1065–1092.

Lord, S. J., H. E. Willoughby, and J. M. Piotrowicz, 1984: Role of a parameterized ice-phase microphysics in an axisymmetric, nonhydrostatic tropical cyclone model. *J. Atmos. Sci.,* **41**, 2836–2848.

McCarthy, J., 1974: Field verification of the relationship between entrainment rate and cumulus cloud diameter. *J. Atmos. Sci.,* **31,** 1028–1039.

Paluch, I. R., 1979: The entrainment mechanism in Colorado cumuli. *J. Atmos. Sci.,* **36,** 2467–2478.

Pontikis, C., A. Rigaud, and E. Hicks, 1987: Entrainment and mixing as related to the microphysical properties of shallow warm cumulus clouds. *J. Atmos. Sci.,* **44,** 2150–2165.

Raga, G. G., J. B. Jensen, and M. B. Baker, 1990: Characteristics of cumulus band clouds off the coast of Hawaii. *J. Atmos. Sci.,* **47,** 338–355.

Raymond, D. J., and M. H. Wilkening, 1982: Flow and mixing in New Mexico mountain cumuli. *J. Atmos. Sci.,* **39,** 2211–2228.

——, and A. M. Blyth, 1986: A stochastic model for nonprecipitating cumulus clouds. *J. Atmos. Sci.,* **43,** 2708–2718.
Reuter, G. W., and M. K. Yau, 1987: Mixing mechanism in cumulus congestus clouds. Part I: Observation. *J. Atmos. Sci.,* **44,** 781–797.
Riehl, H., and J. S. Malkus, 1958: On the heat balance of the equatorial trough zone. *Geophysica,* **6,** 503–538.
Simpson, J., R. H. Simpson, D. A. Andrews, and M. A. Eaton, 1965: Experimental cumulus dynamics. *Rev. Geophys.,* **3,** 387–431.
Sloss, P. W., 1967: An empirical examination of cumulus entrainment. *J. Appl. Meteor.,* **6,** 878–881.
Soong, S.-T., and Y. Ogura, 1980: Response of tradewind cumuli to large-scale processes. *J. Atmos. Sci.,* **37,** 2035–2050.
——, and W.-K. Tao, 1980: Response of deep tropical cumulus clouds to mesoscale processes. *J. Atmos. Sci.,* **37,** 2016–2034.
Squires, P., 1958a: The spatial variation of liquid water and droplet concentration in cumuli. *Tellus,* **10,** 372–380.
——, 1958b: Penetrative downdraughts in cumuli. *Tellus,* **10,** 381–389.
——, and J. S. Turner, 1962: An entraining jet model for cumulonimbus updraughts. *Tellus,* **14,** 3422–3434.
Stommel, H., 1947: Entrainment of air into a cumulus cloud. *J. Meteor.,* **4,** 91–94.
Sui, C.-H., and M. Yanai, 1986: Cumulus ensemble effects on the large-scale vorticity and momentum fields of GATE. Part I: Observational evidence. *J. Atmos. Sci.,* **43,** 1618–1642.
Tao, W.-K., J. Simpson, and S.-T. Soong, 1987: Statistical properties of a cloud ensemble: A numerical study. *J. Atmos. Sci.,* **44,** 3175–3187.
Taylor, B. R., and M. B. Baker, 1991: Entrainment and detrainment in cumulus clouds. *J. Atmos. Sci.,* **48,** 112–121.
Telford, J. W., 1975: Turbulence, entrainment, and mixing in cloud dynamics. *Pure Appl. Geophys.,* **113,** 1067–1084.
Warner, J., 1955: The water content of cumuliform clouds. *Tellus,* **7,** 449–457.
——, 1970: On steady-state one-dimensional models of cumulus convection. *J. Atmos. Sci.,* **27,** 1035–1040.
Xu, K.-M., and S. K. Krueger, 1991: Evaluation of cloudiness parameterization using a cumulus ensemble model. *Mon. Wea. Rev.,* **119,** 342–367.
——, and D. Randall, 1996: Explicit simulation of cumulus ensembles with the GATE Phase III data: Comparison with observations. *J. Atmos. Sci.,* **53**, 3710–3736.
——, A. Arakawa, and S. K. Krueger, 1992: The macroscopic behavior of cumulus ensembles simulated by a cumulus ensemble model. *J. Atmos. Sci.,* **49,** 2402–2420.